

Temporal Evolution of the Light Emitted by a Thin, Laser-ionized Plasma Source

Valentina Lee,¹ Robert Ariniello,² Christopher Doss,¹ Kathryn Wolfinger,³ Peter Stoltz,⁴ Claire Hansel,¹ Spencer Gessner,² John Cary,^{1,5} and Michael Litos¹

¹*Center for Integrated Plasma Studies, Department of Physics, University of Colorado Boulder, Boulder, Colorado 80309, USA*

²*SLAC National Accelerator Laboratory, 2575 Sand Hill Rd, Menlo Park, CA 94025, USA*

³*RadiaSoft LLC, 1790 38th St Suite 306, Boulder, CO 80301, USA*

⁴*Zap Energy, 5901 23rd Dr W Everett, WA 98203, USA*

⁵*Tech-X, 5621 Arapahoe Avenue Suite A Boulder, CO 80303, USA*

(Dated: 20 September 2023)

We present an experimental and simulation-based investigation of the temporal evolution of light emission from a thin, laser-ionized Helium plasma source. We demonstrate an analytic model to calculate the approximate scaling of the time-integrated, on-axis light emission with the initial plasma density and temperature, supported by the experiment, which enhances the understanding of plasma light measurement for plasma wakefield accelerator (PWFA) plasma sources. Our model simulates the plasma density and temperature using a split-step Fourier code and a particle-in-cell (PIC) code. A fluid simulation is then used to model the plasma and neutral density, and the electron temperature as a function of time and position. We then show the numerical results of the space-and-time-resolved light emission and that collisional excitation is the dominant source of light emission. We validate our model by measuring the light emitted by a laser-ionized plasma using a novel statistical method capable of resolving the nanosecond-scale temporal dynamics of the plasma light using a cost-effective camera with microsecond-scale timing jitter. This method is ideal for deployment in the high radiation environment of a particle accelerator that precludes the use of expensive nanosecond-gated cameras. Our results show that our models can effectively simulate the dynamics of a thin, laser-ionized plasma source and this work is useful to understand the plasma light measurement, which plays an important role in the PWFA.

I. INTRODUCTION

Plasma-based accelerators have demonstrated accelerating gradients two to three orders of magnitude larger than conventional radio-frequency accelerators, making them an enticing alternative for future high-energy particle accelerator applications¹⁻³. In a beam-driven plasma wakefield accelerator (PWFA), an electron drive beam generates a wake as it propagates through a plasma. A second electron beam follows the drive beam at a distance on the order of the plasma skin depth. The strong longitudinal electric field of the plasma wake accelerates this “witness” beam. As the performance of a PWFA depends strongly on the plasma density profile⁴⁻⁷, control and understanding of the plasma source are essential to interpret the outcome of experiments and optimize the properties of the plasma source.

A typical PWFA plasma source is a long, narrow filament, 10’s to 100’s of micrometers in diameter and 10’s of centimeters in length, with a core density of $10^{16-18} \text{ cm}^{-3}$. One technique to form a suitable plasma is to laser-ionize a gas using an optic with a long depth of focus, such as an axicon lens or diffractive optic⁸⁻¹¹. In such a plasma source, an $\mathcal{O}(10\text{TW})$, ultrashort laser pulse is focused into a volume of gas, such as Hydrogen, Helium, or Lithium, ionizing a thin filament prior to the arrival of the electron beams. Characterization of the plasma source is often performed in the absence of the electron beams. One common technique is to look at the light emitted by the plasma.

Multiple mechanisms with varying time scales contribute to the plasma light emission process of these thin laser-ionized

plasma sources. The plasma is locally formed on the time scale of the ionizing laser pulse duration, which is around 100 fs. The plasma electrons thermalize within 10 ps of formation. Then, the plasma expands quickly outward within a few nanoseconds while the neutral gas diffuses inward, followed by a slower diffusion and thermalization phase between the plasma and the neutral gas that lasts 10’s to 100’s of nanoseconds. During this time, plasma electrons collide with neutral atoms, exciting them, while also colliding with plasma ions and recombining. Both of these mechanisms contribute to plasma light emission. The latter will also lead to the eventual neutralization of the plasma over a few hundred microsecond time scale¹².

The dynamics of plasma expansion have been studied through simulations and experiments¹³⁻¹⁵, and the electron thermalization time scale has been demonstrated in Ref. 16 and 17. Experimental and theoretical studies of plasma neutralization through recombination are presented in Ref. 18 and 19. However, there remains a gap in understanding the light emission process in thin, laser-ionized plasmas, such as PWFA plasma filaments. The amount of light emitted depends on the electron temperature and the number densities of the plasma and neutral gas. Determining the relative dominance of excitation versus recombination is a complex question influenced by the plasma’s geometry. In this work, we show an analytical and computational model of the plasma light emission process of a thin laser-ionized Helium plasma and confirmed by the experiment.

Our measurements of plasma light emission are taken using an inexpensive camera. These cameras are often used to

verify plasma formation in PWFA experiments. For example, many of the experiments at the Facility for Advanced Accelerator Experimental Tests-II (FACET-II) at SLAC National Accelerator Laboratory rely on cameras to observe the laser-ionized plasma source^{20–26}. Cost-effective cameras, such as Gigabit Ethernet (GigE) machine vision cameras, are typically used in PWFA experiments because the high radiation environment in the accelerator housing leads to rapid cycles of camera failure and replacement. Unfortunately, these cameras have a large trigger timing jitter ($\sim 10 \mu\text{s}$) and long exposure time ($\sim 10 \mu\text{s}$) compared to the short time scales ($10^3\text{s}-100^3\text{s}$ ns) of plasma light emission, making images from these kinds of cameras integrate over various dynamics described previously. In order to verify our model using these cameras, we demonstrate a novel technique to measure the time-resolved light signal using these low-cost cameras.

Our three step light emission model: plasma formation, plasma expansion, and plasma light emission is presented in section II. In section III, we introduce our experimental setup where a laser-ionized Helium plasma is viewed by a GigE machine vision camera. In section IV, we present a novel technique for studying plasma light emission with 1 ns resolution using a low-cost GigE camera. In section V, we demonstrate that the experimental data confirms our Helium plasma light emission model. Furthermore, we show the broad applicability of this diagnostic tool in PWFA experiments by demonstrating that a simple theoretical model can describe the intensity of the plasma light in a time-integrated image, permitting estimation of the initial plasma parameters with a single image of the time-integrated plasma light.

II. MODELING

This section outlines a workflow for modeling the laser-ionized plasma formation, expansion, and light emission. We demonstrate the entire workflow using a single set of parameters (laser pulse duration: $\tau = 50$ fs, focusing optic: 1° axicon lens, laser energy: $E = 160.33$ mJ, gas pressure: $P = 118$ mbar) and compare the time-resolved simulated plasma light emission pattern with experimental data. We also conducted multiple plasma formation simulations for a range of parameters ($E = 140\text{-}175$ mJ and $P = 20\text{-}80$ mbar). The simulated electron temperatures were used to calculate plasma light emission, which is compared to experimental measurements in Section V.

A. Plasma Formation

In a laser-ionized PWFA plasma source, ionization occurs through field ionization, typically in the tunneling regime where the electric field from the laser distorts the atomic potential allowing an electron to tunnel out of the atomic barrier. This process is well described by the ADK model²⁷. Particle-in-cell (PIC) simulations are able to capture this process, however, simulating the ionization process over a 5 ns window (axicon focus of 1.5 m) while resolving the laser period would

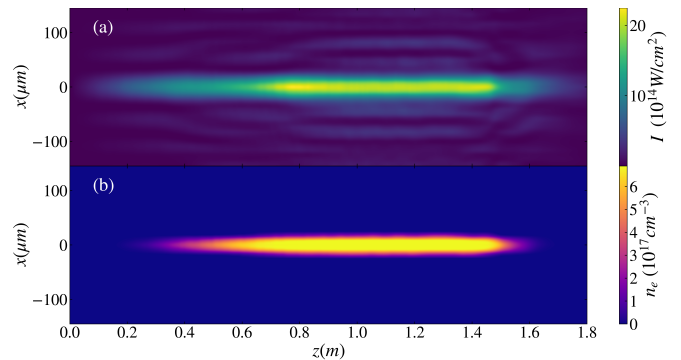


FIG. 1. Simulated formation of an axicon plasma using a split-step Fourier code, with an initial laser pulse energy of 175 mJ in a Helium gas pressure of 28 mbar, corresponding to a fully ionized plasma of $n_e = 6.9 \times 10^{17} \text{ cm}^{-3}$. The axicon lens ($\alpha = 1^\circ$) is positioned at $z = 0$. (a) illustrates the laser intensity at the middle of the pulse on the $y = 0$ plane. (b) shows the plasma density on the $y = 0$ plane. Because of the long Bessel focus from the axicon lens, the full ionization regime extends to up to 1 meter.

require an impractical amount of computational resources. As an alternative, we use an in-house code to simulate the 3D plasma profile produced by the laser. The ADK model is used to calculate the ionization rate; while a the split-step Fourier (SSF) algorithm²⁸ takes into account refraction of the rear of the laser pulse due to the presence of plasma ionized by the front of the laser pulse. Figure 1 shows an example of the simulated laser intensity and plasma density profiles formed by an axicon lens by our SSF code. This code, however, cannot provide information about the initial plasma electron temperature. To accommodate this, we use a PIC code, VSim²⁹ provided by Tech-X, to simulate ionization of a typical localized region along the laser ionization path, importing the local laser pulse profile retrieved from the SSF code. We then extract the plasma electron temperature from the resulting kinetic energy distribution of the electrons in the PIC simulation.

For all PIC simulations in this work, 1 particle per cell is used with a time step of $dt = 3.25 \times 10^{-17}$ s and a spatial increment of $dx = 7 \times 10^{-8}$ m. The transverse size of the simulation box is approximately 14 times the full width at half maximum (FWHM) of the laser's spatial profile, and the temporal dimension is roughly 4 times the FWHM duration of the laser pulse. Modeling ionization through a combination of the SSF and PIC simulations allows us to acquire the plasma density and plasma electron temperature with reasonable computational resources. Figure 2 shows a histogram of the electron kinetic energy distribution as a function of radius. It also demonstrates that the intensity of the ionization laser profoundly influences the azimuthally averaged electron energy. As we will show, our experimental observations confirm that the method described above is a reliable and relatively inexpensive way to model a laser-ionized PWFA plasma source.

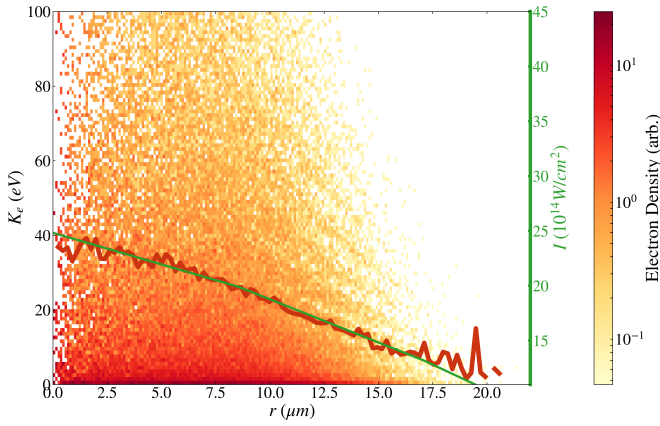


FIG. 2. The plot illustrates the plasma electron energy histogram as a function of the radius, ionized by a 175 mJ pulse in Helium gas with a density of $6.9 \times 10^{17} \text{ cm}^{-3}$, simulated by a PIC simulation. The azimuthally averaged radial electron energy is represented by the red curve and the ionizing laser intensity is represented by the green curve. The azimuthally averaged radial electron energy follows the intensity of the ionization laser.

B. Plasma Expansion

The plasma electrons thermalize on the order of the Spitzer electron self-collision time, given by $\tau \approx (1.40/(8\pi r_e^2 c^4 n_e \ln \Lambda))(3k_B T_e/m_e)^{3/2}$ where r_e is the classical electron radius, c is the speed of light, n_e is the plasma electron density, $\ln \Lambda$ is the Coulomb logarithm, k_B is the Boltzmann constant, T_e is the average electron temperature, and m_e is the mass of electron³⁰. For example, for a plasma with $k_B T_e = 10 \text{ eV}$ and $n_e = 1 \times 10^{17} \text{ cm}^{-3}$, $\tau \approx 9 \text{ ps}$. This fast thermalization process has been measured in Ref. 16 and 17. The thermalized electron temperature of the plasma is $k_B T_e = 2/3 \langle E_k \rangle$, where $\langle E_k \rangle$ is the average electron kinetic energy immediately after ionization. The expansion of a laser-ionized plasma source can be modeled using fluid simulations, as demonstrated in Ref. 13. Using the plasma density profile and the plasma electron temperature acquired from previous steps, we model the plasma expansion using Tech-X's fluid simulation software, USim. USim is an Eulerian computational fluid dynamics code optimized for plasma fluid simulations by solving the Magnetohydrodynamic (MHD) equations³¹. We simulate the first 3 ns of the expansion using a two-temperature, single-fluid MHD diffusion code, where the ion temperature is 0.025 eV (300 K) and the average electron temperature is taken from the PIC simulation, $\langle T_e \rangle \sim 13 \text{ eV}$. The simulated expansion is shown in figure 3(a). For the subsequent expansion from 3 ns until $t = 200 \text{ ns}$, plasma-neutral collisions are accounted for using a two-fluid model that calculates the mass diffusion, energy exchange, and temperature exchange between two species (plasma and neutral)^{32,33}. The subsequent expansion is shown in Fig. 3(b). It has been tested that the results of the second simulation period are relatively insensitive to the exact choice of the transition time, so long as the change in density is relatively small. As shown by the red curve (density lineout) in Fig. 3(a), the expansion (decay)

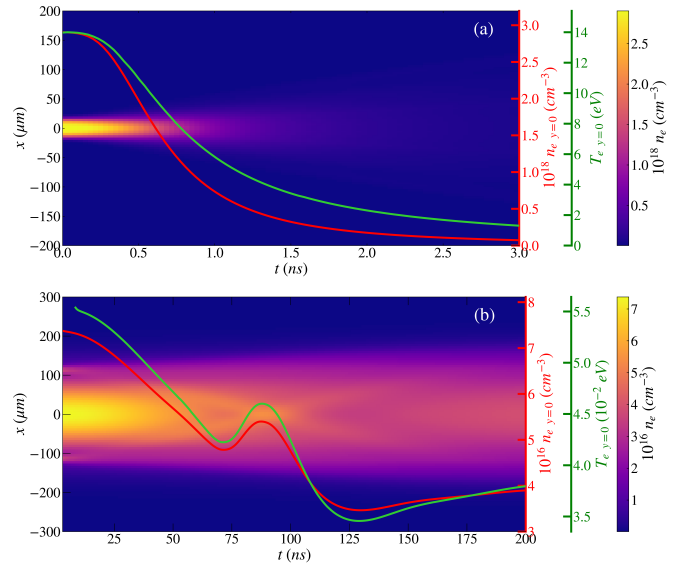


FIG. 3. Simulated plasma expansion using fluid codes. (a) shows the plasma expansion on the $y = 0$ plane within the first three nanoseconds simulated by a single-fluid MHD model. (b) shows the plasma expansion on the $y = 0$ plane from the 3 ns to 200 ns, including plasma-neutral collision effects. In both figures, the red and green curves show the plasma density (n_e) and plasma temperature (T_e) at $x = 0$, respectively. Note that the first 5 ns (numerical thermalization time) of the green curve (T_e) in (b) is excluded from the plot.

reaches $1/e^2$ before 3 ns. Simulating the expansion in two steps simplifies the complexity of the model and allows for a higher temporal resolution during the initial rapid expansion.

C. Plasma Light Emission

Light emission from plasma can be generated by two primary processes: electron-neutral collisional excitation and plasma electron-ion recombination. Both processes are intricate and require Monte Carlo atomic electron tracking models³⁴ to simulate exactly, which is both theoretically and computationally demanding. To simplify the problem, we focus on the most probable transition process that emits visible/NIR light in either process, since that is what Complementary Metal-oxide Semiconductor (CMOS) GigE camera can detect.

In the collisional excitation model, the electrons have a significantly higher temperature ($T_e \sim 15 \text{ eV}$) compared to the ions and neutrals ($T_i \approx T_n \sim 0.025 \text{ eV}$). Therefore, electron-neutral collisions dominate while ion-neutral and neutral-neutral collisions are negligible. We also assume that all neutral atoms are in their ground state before the collision. In a Helium atom, $3d - 2p$ de-excitation has the strongest persistent lines. The dipole-allowed transitions from the ground state occur from the $1s$ ($l = 0$) state to the p ($l = 1$) states. Of these, excitation to the $4p$ state has the largest cross-section among allowed excited states that can generate a visible/NIR photon from a subsequent $3d - 2p$ de-excitation. Therefore, we choose this $1s - 4p - 3d - 2p$ excitation/de-excitation pro-

cess to calculate the lower bound of the visible photon emission rate via a single excitation path. Appendix A presents a more detailed explanation of this model. To calculate the local excitation rate per unit volume, we start with the collision rate for one electron with a population of neutral particles^{35–37},

$$v_{en} = n_n \sigma(v)_{1s-4p} v, \quad (1)$$

where n_n is the local neutral density, $\sigma(v)_{1s-4p}$ is the electron-impact excitation cross-section from the 1s state to the 4p state, and v is the relative velocity between the electron and the neutrals, which is approximated as the electron velocity ($v_e \gg v_n$). The probability density function for a given speed ($v = |\vec{v}|$) for a Maxwellian population of electrons is

$$f(v) = \left(\frac{m_e}{2\pi k_B T_e} \right)^{3/2} 4\pi v^2 \exp\left(-\frac{m_e v^2}{2k_B T_e}\right), \quad (2)$$

where $\int_0^\infty f(v) dv = 1$. The average collision rate per electron is

$$\begin{aligned} \langle v_{en} \rangle &= \frac{\int_0^\infty f(v) n_n \sigma(v) v dv}{\int_0^\infty f(v) dv} \\ &= n_n 4\pi \left(\frac{m_e}{2\pi k_B T_e} \right)^{3/2} \int_0^\infty \exp\left(-\frac{m_e v^2}{2k_B T_e}\right) \sigma(v) v^3 dv. \end{aligned} \quad (3)$$

This average collision rate can be written in terms of the kinetic energy, K :

$$\begin{aligned} \langle v_{en} \rangle &= \frac{8\pi n_n}{m_e^2} \left(\frac{m_e}{2\pi k_B T_e} \right)^{3/2} \\ &\int_0^\infty \exp\left(-\frac{K}{k_B T_e}\right) \sigma(K) K dK. \end{aligned} \quad (4)$$

Thus, the excitation rate per unit volume at location \vec{r} and time t , for a population of electrons colliding with a population of neutrals is $n_e \langle v_{en} \rangle$, which depends on \vec{r} and t through n_e , n_n , and T_e .

After the collisional excitation, some excited electrons in the 4p state spontaneously de-excite to the 3d state, and then to the 2p state, yielding a detectable photon emission. The decay transition probability from state i to state j is

$$P_{ij} = \frac{A_{ij}}{\sum_k A_{ik}}, \quad (5)$$

where k indicates all dipole-allowed final transition states from initial state i , and A is the transition rate, here taken from Ref. 35.

The transition probability from the 4p state to the 3d state is $P_{4p-3d} \approx 1.2 \times 10^{-3}$, and from the 3d to the 2p state is $P_{3d-2p} \approx 1$. The visible photon emission rate is thus

$$\frac{dn_{\gamma_{exc}}(\vec{r}, t)}{dt} = n_e(\vec{r}, t) \langle v_{en}(\vec{r}, t) \rangle P_{4p-3d} P_{3d-2p}.$$

We then proceed to work out an analytic prediction of the peak photon emission ($x = 0, y = 0$) scaling as a function of

the initial plasma density and temperature with a few assumptions explained in Appendix B:

$$\begin{aligned} \Gamma &= \int_0^\infty n_e(x=0, y=0) \langle v_{en}(x=0, y=0) \rangle dt \\ &= C n_0^2 \sqrt{R k_B T_0} \exp\left(-\frac{K_{th}}{R k_B T_0}\right), \end{aligned} \quad (6)$$

where C is scaling constant left as a free parameter to fit to the data, n_0 and T_0 are the initial electron density and temperature at $x = 0, y = 0$, respectively, K_{th} is the free electron kinetic energy threshold for exciting a ground-state atom to the 4p state, and $R = 0.09$ is the empirically acquired temperature decay ratio; that is, the ratio between the initial temperature and the final temperature after the initial fast expansion as shown in Fig. 3 (a). This value was obtained from our simulation and may vary in other circumstances, though it agreed well with the experimental data over a relatively wide range of initial plasma parameters. The detailed derivation of 6 can be found in Appendix B.

The other possible light emission process, recombination, can occur through three different primary modes: three-body recombination, radiative recombination, and dielectronic recombination³⁸. Radiative recombination dominates the production of visible photons³⁹, wherein a single free electron recombines with a singly ionized ion into one of its high Rydberg states, yielding a highly-excited Helium atom. The rate of electron-ion radiative recombination can be approximated as follows⁴⁰:

$$\alpha_r = 2.7 \times 10^{-13} Z^2 T_e [eV]^{-1/2} [\text{cm}^3/\text{s}], \quad (7)$$

where $Z = 1$ is the charge state of He^+ . The recombination rate⁴¹ is, therefore,

$$\frac{dn_{\gamma_{rec}}}{dt} = \alpha_r n_e^2, \quad (8)$$

assuming quasi-neutrality.

Because it is more energetically favorable, we assume that most of the recombined electrons start in a highly-excited state and then eventually de-excite to the ground state in a radiative process. To estimate an upper bound of the detectable photon emission rate from a single recombination event, we look at the strongest visible/NIR line in Helium atoms, the 3d – 2p transition. We then assume that electrons in high Rydberg states eventually go through the dominant transition process, 4f – 3d – 2p^{35,42}. The details of the model are discussed in Appendix A. The de-excitation transition probability for 4f states to 3d states is $P_{4f-3d} \approx 1$. The local visible photon emission rate from electron-ion recombination is thus

$$\frac{dn_{\gamma_{rec}}(\vec{r}, t)}{dt} = \alpha_r n_e(\vec{r}, t)^2 P_{4f-3d} P_{3d-2p}. \quad (9)$$

Note that 9 is predicated on the assumption that all recombination events lead to the emission of a detectable photon, which is not strictly true, but does provide an upper-bound estimation of the recombination photon emission rate.

The collisional excitation and recombination rates per unit volume are orders of magnitude less than the electron density, so their effects on the expansion of the plasma are negligible. This allows us to model the time-resolved plasma expansion first and then numerically estimate the visible photon emission density from excitation and recombination using Eq. 6 and Eq. 9 at each moment in time, t , and at every position, \vec{r} . The cross-section in Eq. 1 is numerically interpolated from Ref. 43. Our simulation indicates that the visible/NIR photon emission rate from the collisional excitation is three orders of magnitude greater than that from recombination. Recall that in our estimation, the photon emission rate arising from collisional excitation is a lower bound, while that from plasma recombination is an upper bound. Thus, even with the simplifications introduced in our model, the assertion that collisional excitation principally dominates the light emission process remains valid. Figures 8 (a) illustrates the time-resolved simulated photon emission pattern from an expanding Helium plasma.

III. EXPERIMENTAL SETUP

The plasma channel is ionized by a 50 fs, 450 mJ pulse from a terawatt-class Ti:Sapphire laser system. The wavefront of the pulse is optimized with a deformable mirror before being sent through an axicon lens ($\alpha = 1^\circ$) that generates a non-diffracting Bessel-beam focus over a length of ~ 150 cm. The experimental vacuum chamber is filled with Helium gas, creating the plasma source within. The vacuum system consists of two vacuum chambers connected with vacuum pipes and a six-way vacuum cross as shown in Fig. 4. The plasma is formed inside the vacuum pipe and viewed through an optical window. The gas pressure is monitored by a vacuum gauge and recorded on a shot-by-shot basis. The laser intensity profile is recorded upstream and downstream of the axicon lens. The former is used as an input parameter for the simulation, and the latter is used to monitor the Bessel focus profile.

The diagnostic system views the plasma light at 1 m downstream of the axicon. A commercial camera lens (AT-X M100 PRO D Macro from Tokina, $f = 100$ mm) is installed immediately outside the vacuum window. A 6-OD notch filter (central wavelength= 785 nm, FWHM= 33 nm) filters out most of the scattered laser light that appears as a background to the plasma light. The imaged plasma light is recorded with a CMOS GigE camera chip (Sony IMX265), forming the primary source of data collected in this experiment.

The camera is externally triggered by a trigger pulse train from a Signal Delay Generator (SDG), which is synchronized with the Ti:Sapphire laser system. The timing of the laser system is precise to the sub-picosecond scale; the SDG is precise to the 10's of picoseconds scale. However, the CMOS GigE camera has a significant internal timing jitter between the arrival of the trigger signal to the initiation of the exposure time, on the scale of $10 \mu\text{s}$. The shortest integration time for this type of camera is on the order of $10 \mu\text{s}$, whereas the dynamic timescale of light emission from the plasma is 10's to 100's of nanoseconds. Therefore, this type of camera always cap-

tures a time-integrated signal of the plasma light that is much longer than the dynamic timescale.

Despite the limitations of CMOS GigE cameras, their cost-effectiveness makes them a preferred choice in high-radiation environments. For example, in the FACET-II accelerator tunnel at SLAC National Accelerator Laboratory, approximately 10 GigE cameras are employed solely to monitor the laser and plasma source. During operations, FACET has reported the loss of more than 20 cameras per year due to high radiation exposure. Therefore, cost-efficient CMOS cameras (typically a few hundred dollars each) are far more suitable than would be a fast (nanosecond) gated camera, which can cost tens of thousands of dollars. In Section IV, we introduce an innovative analysis method to extract time-resolved plasma light emission data from time-integrated measurements using inexpensive GigE cameras.

IV. ANALYSIS METHODOLOGY

A. Statistical Analysis

As explained in the previous section, CMOS GigE cameras are preferable in high-radiation environments but are conventionally unsuitable for high-timing-precision measurements. In this section, we discuss an inventive statistical analysis to extract time-resolved light emission from multi-shot time-integrated data.

The first step is quantifying the camera-trigger-jitter distribution, which is device-dependent. Physically, a trigger pulse is sent at time t_{SDG} to the GigE camera. After processing in the camera chip, the exposure time begins at t_{start} . This delay between t_{SDG} to t_{start} varies shot-to-shot; we call this the camera-trigger-jitter, which follows a distribution $J(t)$. The precision of the laser arrival time at the target plasma location ($\mathcal{O}(10\text{ps})$) is orders of magnitude smaller than the camera-trigger-jitter ($\mathcal{O}(10\mu\text{s})$). As a result, the laser arrival time can serve as a fiducial signal to investigate $J(t)$. The diagnostic camera is first synchronized to the laser arrival-time, so that the laser pulse always arrives within the duration of the camera exposure time and the laser scattered light is captured by the camera in every shot. This starting time is defined as $t = 0$ in Fig. 5. The trigger signal is then advanced/delayed away from $t = 0$. Because the exposure starting-time (and ending-time) jitters, the laser pulse will sometimes fall outside the exposure window as the delay time is scanned, resulting in images without laser signal. Eventually, the trigger advance/delay is great enough that none of the images taken capture the laser. The observed probability of a laser pulse falling inside the camera exposure window as a function of advance/delay time, $j(t)$, is plotted in Fig. 5. Note that the falling edge in this figure corresponds to a relative *delay* of the SDG trigger, meaning that the laser arrives *ahead* of the camera exposure's starting-time. This implies that the falling edge of $j(t)$ is the cumulative distribution function of the camera-trigger-jitter distribution, $J(t)$,

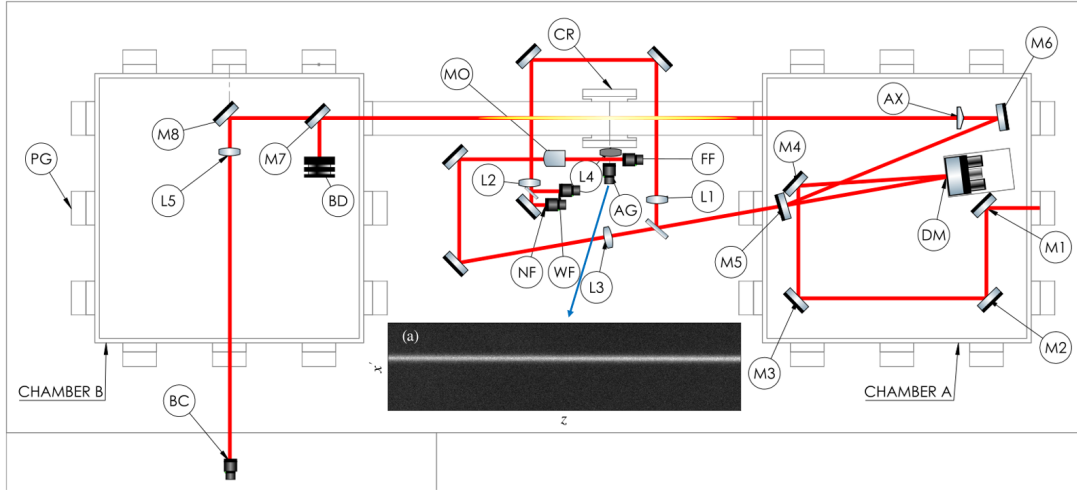


FIG. 4. Experimental setup. 50 fs laser pulses generated by a Ti:Sapphire laser system enter Chamber A through the rightmost window in this figure, bouncing off mirrors M1, M2, M3, M4, and the deformable mirror (DM). The leakage light from M5 exits the vacuum chamber and splits into three paths to the near-field camera (NF), far-field camera (FF), and the Shack-Hartmann wavefront sensor (WF) to monitor the laser position, pointing, and wavefront. (L1, L2: lenses; MO: microscope objective.) The main laser beam reflects off mirrors M5 and M6, passing through a 1° axicon lens (AX), which produces a Bessel focus within the vacuum pipe between Chamber A and Chamber B. The Bessel focus is centered at the six-way cross (CR), as denoted by the yellow region indicating plasma formation. The laser beam is terminated at the beam dump (BD), while the leaked light from mirror M7 is used for imaging the Bessel focus by a single lens (L5) to a camera (BC). On the diagnostic side, a commercial macro lens (L4) is used to image the plasma light onto a camera (AG). The vacuum pressure is measured shot-to-shot using a pressure gauge (PG) on the figure’s far left. (a) shows an example of the raw plasma light image taken by camera AG.

$$j(t) = \int_{-\infty}^t J(t) dt. \quad (10)$$

The cumulative distribution function of a normal distribution is

$$j(t) = \frac{1}{2} \left(1 + \operatorname{erf} \left(\frac{t - \mu_J}{\sigma_J \sqrt{2}} \right) \right), \quad (11)$$

where μ_J is the mean of $J(t)$, σ_J is the deviation of $J(t)$, and erf is the error function. The rising and falling edge data presented in Fig. 5 is fitted with Eq. 11 and the camera-trigger-jitter distribution, $J(t)$, is thus determined from Eq. 10, assuming normal distribution and σ_J is given by the fitting, and plotted in Fig. 6

The observable plasma light lasts for an extended duration of time dt_{glow} . Most of the images captured by the camera either include both the plasma light and background light from the laser pulse, or neither. (Note: Though the notch filter removes much of the scattered laser light, some always remain visible on the camera.) For certain trigger delay times, however, it is possible for the camera to capture a portion of the plasma light while the prompt laser light falls outside of the camera’s exposure window. This happens when the exposure begins after the laser arrives but before the plasma light ends. The longer the plasma light decay time, dt_{glow} , the more these “lucky shots” accumulate.

The purple area under the curve in Fig. 6 represents these “lucky shots” (shots with plasma light but without the laser signal). The ratio of “lucky shots” to all recorded shots R is expressed as

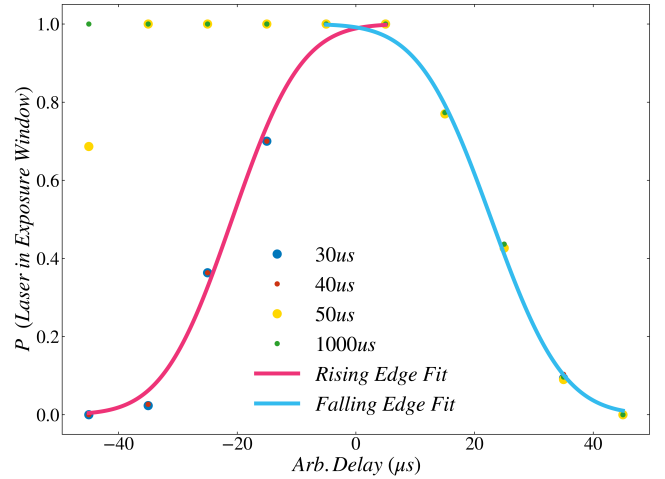


FIG. 5. Measurement of the probability of a laser pulse appearing within the camera’s exposure time at various relative delays, measured with 30, 40, 50, and 1000 μs exposure settings. Jitter of the camera’s exposure start time and end time cause the falling and rising ramps to be continuous functions instead of step functions. Repeatable measurements of the falling edge at the various exposure settings (30, 40, 50, and 1000 μs) confirm that altering the exposure duration does not affect the start-time jitter. The magenta and cyan curves show Eq. 11 fitted to the rising and falling ramps, respectively.

$$R = \int_{t_{\text{laser}}}^{t_{\text{laser}} + dt_{\text{glow}}} J(t - t_{\text{SDG}}) dt \quad (12)$$

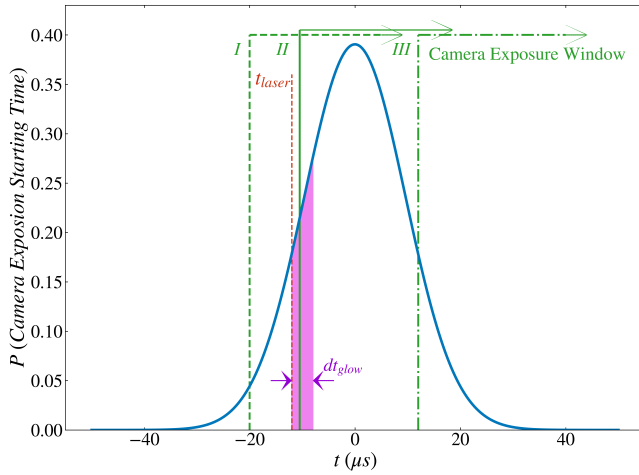


FIG. 6. A conceptual diagram illustrating the relationship between camera jitter, laser arrival time, and plasma light time scale. The blue curve represents the camera starting time jitter distribution measured and calculated by Eq. 10. The red dashed line indicates the laser arrival time. Following the laser arrival, if a plasma is formed, the plasma light continues to glow for an extended duration, dt_{glow} , until the intensity is undetectable. This is represented as the purple area shown in the figure, though the scale of dt_{glow} is greatly exaggerated for illustration. When the camera exposure starts at time *I* (dashed green line), the captured image contains both laser and plasma light. When it starts at time *III* (dot-dashed green line), no light is captured in the image. However, when it starts at a propitious timing, *e.g.*, at time *II* (solid green line), the camera exposure begins after the arrival of the laser but before the plasma light dissipates, resulting in the capture of only the plasma light without the laser light.

where $J(t - t_{\text{SDG}})$ is the camera-trigger-jitter distribution centered about a given SDG trigger time t_{SDG} , and $t_{\text{laser}} \equiv t_{\text{SDG}_0}$, where t_{SDG_0} is the timing $t = 0$ at Fig. 5. Accordingly, we solve for dt_{glow} , giving

$$dt_{\text{glow}}|_{t_{\text{SDG}}} = \frac{-J(t_{\text{laser}}) + \sqrt{J(t_{\text{laser}})^2 - 2I J'(t_{\text{laser}})}}{J'(t_{\text{laser}})} \Big|_{t_{\text{SDG}}} \quad (13)$$

where J' denotes the time derivative of J , and $I = R \int_{-\infty}^{\infty} J(t - t_{\text{SDG}}) dt$. Using Eq. 13, we can measure the characteristic plasma emission time scale without a nanosecond gated camera, so long as we record a statistically sufficient number of images with our GigE camera.

B. Data Processing

In this subsection, we explain how the raw experimental data is processed before performing the statistical analysis described in the previous subsection. We collected data at various SDG delays across a $120 \mu\text{s}$ interval with $10 \mu\text{s}$ increments. For each SDG delay, we set the camera exposure time to 30, 40, 50, and $1000 \mu\text{s}$. We captured 300 shots for each combination of SDG delay and exposure time, resulting in a total of 12,000 data shots.

Scattered laser light fills the vacuum chamber during the experiment, resulting in plasma light emission images with high background noise at the laser frequency. The background noise level is hundreds of times higher for shots that include prompt laser light than for those that do not, making it easy to identify shots where the laser arrival time fell within the camera exposure window.

Due to the high and fluctuating noise level, distinguishing the plasma signal from the background noise is somewhat challenging. A dynamic statistical threshold is employed to determine whether any particular image includes a signal from plasma emission light. A region of interest where the plasma light may appear is identified as the “plasma region” and the rest of the image is tagged as the “background region”. We work out the 99.7% error bound for a population mean (EBM), that is, the probability of the average of a random sample falling below $\bar{x}_{\text{max},99.7}$ is 99.7% based on

$$\bar{x}_{\text{max},99.7} = \bar{x} + z_{99.7} \frac{\sigma}{\sqrt{n}}, \quad (14)$$

where $z_{99.7} = 2.778$ is the Z score for 99.7% probability, \bar{x} is the average light count value of the “background region”, σ is the standard deviation of the “background region”, and n is the sample size of the “plasma region”. When the average value of the “plasma region” exceeds the threshold defined in Eq. 14, it is considered a positive signal of plasma light emission. This dynamic statistical threshold effectively adapts to the varying background intensities and is more efficient than a fixed intensity threshold.

By Eq. 13, we determined that the decay time scale of the detectable signal for our laser-ionized Helium plasma light emission is $194 \pm 14 \text{ ns}$. We identified 204 shots that exhibited plasma light emission without laser light based on Eq. 14. Each image is rotated to ensure the plasma light filament appears completely horizontal. Since the plasma filament is homogeneous over the majority of its length, we took the projection of these images along the laser propagation axis and plotted them as a waterfall plot in Fig 7(a), sorted by total intensity of the region of interest. Each column in the waterfall plot represents one plasma-light-only shot. Because the camera exposure window starts at t_{start} , which is after the arrival of the laser pulse, t_{laser} , the plasma light in each shot is integrated from t_{start} to the end of the detectable light emission, $t_{\text{endEmission}}$. Since the decay time scale of the plasma light is orders of magnitude shorter than the characteristic camera jitter time scale, the 204 plasma-light-only shots can be treated as being roughly uniformly distributed in time within the 194 ns plasma light emission window, yielding an effective time resolution of approximately 1 ns.

Every column in Fig. 7 corresponds to an integrated plasma light signal from t_{start} to $t_{\text{endEmission}}$, (where t_{start} shifts $\sim 1 \text{ ns}$ further away from t_{laser} from one column to the next), thus subtracting each column from its neighboring column yields a time-resolved plasma light emission plot with a resolution of $\sim 1 \text{ ns}$. We apply a Gaussian noise filter to the waterfall plot in Fig. 7 (a), then subtract one column from the next to yield the time-resolved plasma light emission pattern shown in Fig. 7 (b). The results of this analysis demonstrate the ability

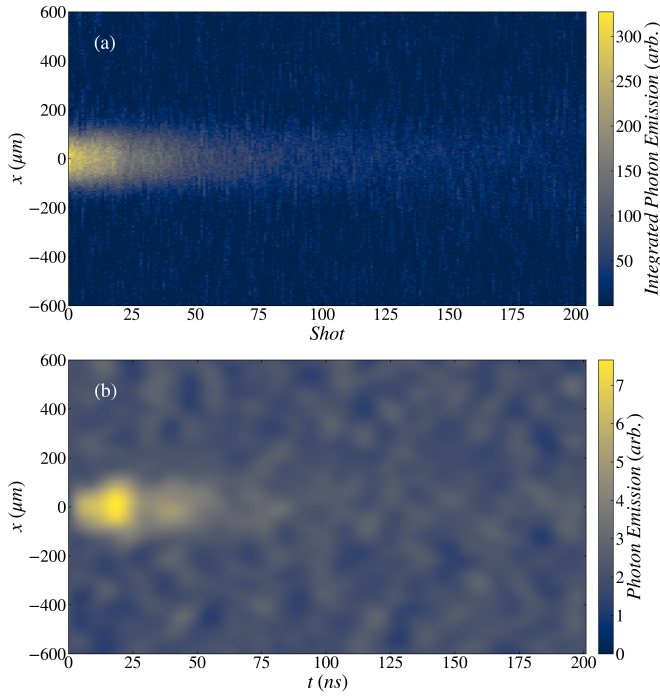


FIG. 7. Each column in (a) represents a single image (shot) containing plasma light but without a laser signal. The images have been summed over the laser/plasma axial dimension. The columns are sorted and aligned based on their total intensity within the region of interest. Each image integrates from $t = t_{start}$ to $t_{EndEmission}$. In the shot with the highest intensity (leftmost column), $t_{start} \sim t_{laser}$; whereas in the rightmost column, $t_{start} \sim t_{EndEmission}$. (b) shows the result after a Gaussian (low-pass) filter is applied to (a) and each column is subtracted from the next column, yielding time-resolved (spatially integrated) photon emission profile with the temporal resolution ~ 1 ns.

to achieve $\mathcal{O}(1$ ns) time-resolved imagery of the plasma light using a cost-effective GigE CMOS camera.

Finally, The camera records the light emission function projected along the camera axis, the radial emission function is retrieved with Abel inversion⁴⁴, as shown in Fig. 8 (b).

V. RESULTS AND DISCUSSION

We compare the results of our simulation work and our experimental data analysis in Fig. 8, and observe good agreement overall. Figure 8 (a) and (b) show the time evolution of the simulated and experimentally observed plasma light emission along the x axis ($y = 0$) at an arbitrary z location within the homogeneous middle region of the plasma filament, respectively. The simulations used to generate Fig. 8 (a) are described in section II, and the data analysis methods lead to Fig. 8 (b) is described in Section IV B. Figure 8 (a) and (b) are normalized for comparison.

Figure 8 (c) shows the photon emission density from Fig. 8 (a) and (b) at the center location ($x = 0, y = 0$) as a function of time. We see good agreement, including the approximate time of the second peak in brightness between 75 and 100

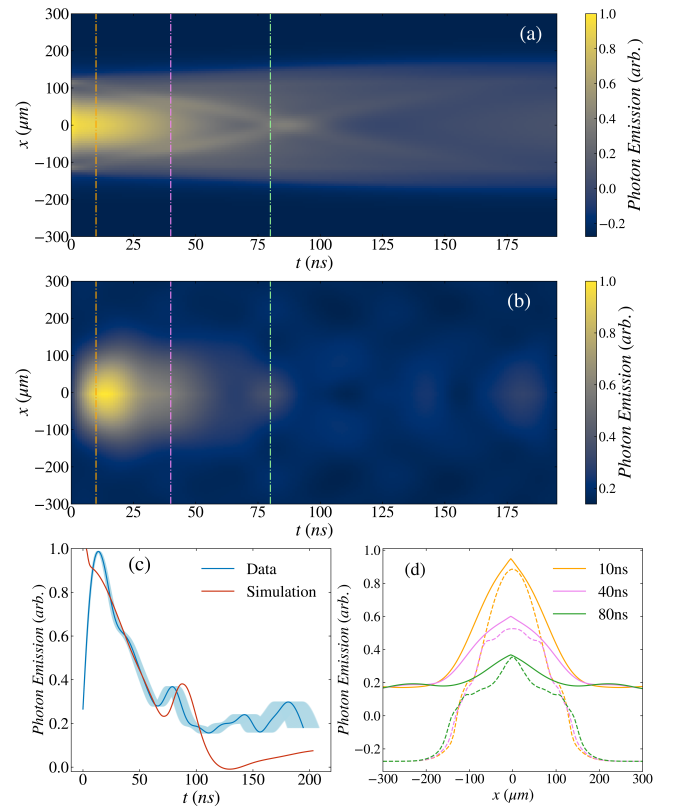


FIG. 8. Light emission from the plasma as a function of radius and time from (a) simulation and (b) measurement. Measurements were taken at $z = 1$ m from the axicon. (c) shows the temporal evolution at $r = 0$ with simulation in red and experimental data in blue. The shaded region is the statistical temporal measurement error. (d) shows radial lineouts at 10, 40, and 80ns, solid lines are experiment and dashed lines simulation.

nanoseconds. There is a slight discrepancy in the first 10 ns, where the data shows a sharp rise from zero, and the simulation immediately yields a high photon emission density. This is due to the fact that the model we used in our simulation does not take into account the atomic decay lifetime of the excited atoms, which leads to a slight delay between the formation of the plasma and the onset of photon emission. The lifetime of the $4p$ state is 3.975 ns and the $3d$ state is 15.696 ns³⁵, which qualitatively matches the delayed peak observed at 13.5 ns.

Figure 8 (d) compares the full photon emission density profile along x at a few different times, 10, 40, and 80 ns. We again see generally good agreement, though the data does not seem to capture the ~ 400 μm -wide diffuse region of light at later times. This is likely an artifact of our limited signal-to-noise ratio in the experimental data, and the noise level can be observed in Fig 8 (c) as well after ~ 100 ns.

Lastly, Figure 9 (a) and (b) show the experimental results of a laser energy scan and a gas pressure scan, respectively. The data points of each plot correspond to the peak photon emission observed in the *time-integrated* (*i.e.* the entire plasma light lifetime falls within the camera integration time), spatially resolved data (average of 100 shots). The lines corre-

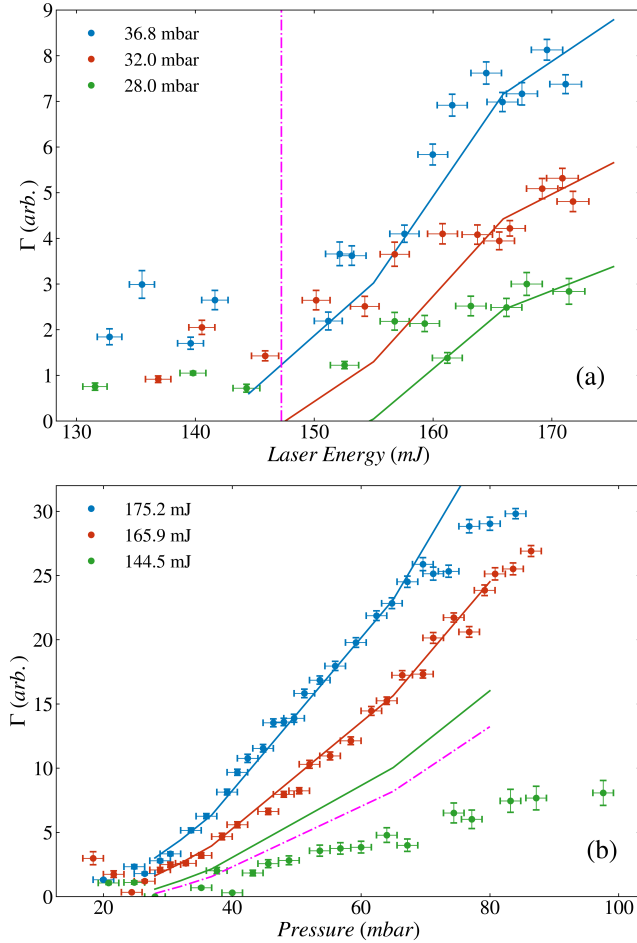


FIG. 9. Time-integrated peak photon emission as a function of (a) laser energy and (b) gas pressure. Each data point represents the average result of 100 measurements. The solid lines show the calculated quantity from Eq. 6, where T_e is simulated using PIC simulations and n_0 is assumed to correspond to a fully ionized gas at the given pressure. The purple dot-dashed line in (a) shows the laser energy at which 99% ionization occurs, approximately 147 mJ. The purple dot-dashed line in (b) shows the curve corresponding to calculation at which 99% ionization occurs, below which the gas is not expected to be fully ionized. The analytic formula agrees well with the data when the plasma is fully ionized.

spond to an analytic prediction of the temporally integrated peak photon emission, Γ , using Eq. 6. Despite the complexity of the plasma light emission process, the experimental data shows remarkable agreement with our simple prediction of the peak photon density scaling as a function of the initial plasma parameters, n_0 and T_0 .

VI. CONCLUSIONS

We have demonstrated an experimental comprehension of the decay process of the plasma light emitted from a thin, laser-ionized Helium plasma source, supported by numerical simulations. We used a three-step model to model the pho-

ton emission pattern, which showed that electron-neutral collisional excitation dominates over electron-ion recombination. The photon emission pattern was measured in the experiment from a $6.9 \times 10^{17} \text{ cm}^{-3}$, $\sim 30 \mu\text{m}$ wide plasma and agrees well with the simulation. We constructed an analytic model to predict the scaling of the time-integrated, on-axis light emission with the initial plasma density and temperature according to Eq. 6 and we saw the expected scaling in the experiment.

We also presented a novel statistical approach for measuring the temporal evolution of plasma light with nanosecond resolution using a cost-effective GigE CMOS machine vision camera. By leveraging the prompt scattered laser light as a fiducial signal, we quantified the exposure timing jitter distribution of the camera and measured the observable plasma light lifetime at $194 \pm 14 \text{ ns}$. Furthermore, by sorting and applying image processing techniques, we reconstructed the time-resolved plasma light emission profile with nanosecond-level precision.

This statistical method is generalizable and offers new diagnostic possibilities in PWFA experiments and related applications where cost-effective diagnostics are a necessity. To prove effective, there must exist an appropriate temporal fiducial signal (e.g. prompt laser light) and the the detector's timing jitter distribution must exhibit statistical repeatability. In PWFA experiments, these two requirements are often met due to the presence of a laser and an electron beam, which can serve as reliable temporal fiducial signals. This technique allows commonly used sensors to achieve measurements previously exclusive to expensive gated sensors (e.g. gated cameras or gated spectrometers) on a statistical basis, giving inexpensive GigE CMOS cameras access to nanosecond dynamics. For example, this technique could be applied to Stark broadening of emission lines in the plasma glow⁴⁵ detected by a spectrometer; a CMOS camera equipped with a wide-angle lens can capture the formation of laser-ionized meter-scale plasma. Some potential applications in PWFA include imagining the dissipation of the plasma wake⁴⁶, investigating the plasma heating mechanism by an electron beam for laser-electron alignment purposes⁴⁷, and measuring the recovery time of a plasma-wakefield accelerator⁴⁸.

Finally, we come to two more significant conclusions regarding the work presented here. First, our results enhance our confidence in the validity of the plasma formation models. In particular, we have confirmed that the relatively inexpensive SSF simulation is able to accurately predict the laser ionization process, making it a valuable tool in the iterative plasma source design process. Second, our advances in understanding of the readily accessible plasma light emission have enhanced its utility as a diagnostic tool. Numerous studies have shown that the electron temperature of the PWFA-like plasma source impacts a wide range of applications^{49–51}, and the methods described in our work can make it possible to design and diagnose experiments that aim to study such effects with significantly greater confidence.

ACKNOWLEDGMENTS

This material is based upon work supported by the U.S. Department of Energy, Office of Science, Office of High Energy Physics under Award No. DE-SC0017906 and the National Science Foundation under Grant Number PHY-2047083.

Appendix A: Excitation and recombination model

Detectable visible/NIR photons are emitted by transitions in Helium between the $n = 3$ and $n = 2$ energy levels. Among these transitions, the $3d - 2p$ transition exhibits the highest rate and the most persistent atomic spectral line of neutral Helium³⁵. Consequently, our focus is on processes that populate the $3d$ state. To populate the $3d$ state, electrons can transition from p or f states. Although the $4f - 3d$ transition has a higher transition than the $4p - 3d$ transition, populating the f states requires a higher excitation energy, which corresponds to a significantly smaller collisional cross-section. Therefore, in a collisional excitation scenario, the most probable transition from the ground state that will yield a visible/NIR photon is the sequence $1s - 4p - 3d - 2p$.

On the other hand, in plasma electron-ion recombination, it takes less energy to capture a free electron into a highly excited state⁵². As a result, most recombination events result in highly excited states, thereby easily populating the $4f$ state. Therefore, in a recombination and de-excitation process, the most probable transition leading to a visible/NIR photon is $4f - 3d - 2p$.

Appendix B: Temporally integrated peak photon emission density

The analytic formalism for the temporally integrated peak photon emission is derived by integrating $n_e \langle v_{en} \rangle$ from $t = 0$ to $t = \infty$ with a few key approximations and assumptions. Recall $\langle v_{en} \rangle$ is given by Eq. 4. We note that the peak photon emission occurs at $\bar{r} \simeq 0$ and for simplification, we drop the notation $\bar{r} \simeq 0$. To calculate the integral in Eq. 4, we first plot the electron-impact excitation cross-section from Ref. 43 in Fig. 10, and fit it with the following function:

$$\sigma(K)_{1s-4p} = A(K - \kappa - K_{th}) \exp\left(-\frac{K}{K_w}\right) + \psi, \quad (\text{B1})$$

where $A = 2.1 \times 10^{-4} \text{ cm}^2$, $\kappa = 34.2 \text{ eV}$, $K_w = 26 \text{ eV}$, $\psi = 7.5 \times 10^{-3} \text{ cm}^2$ are the free parameters found by the fit. The integral in Eq. 4 becomes

$$I_{exc} \approx A \int_{K_{th}}^{\infty} \exp\left(-\frac{K}{k_B T_e(t)}\right) \left((K - \kappa) \exp\left(-\frac{K}{K_w}\right) + \psi \right) K dK. \quad (\text{B2})$$

Because the electron temperature during the plasma glowing process (as shown in Fig. 3 (b)) is orders of magnitude less

than the initial temperature, we make the following approximations, $K_{th} \gg k_B T_e$, $C \gg k_B T_e$, and $B \gg k_B T_e$. The integral now becomes

$$I_{exc} \approx A k_B T_e(t) \exp\left(-\frac{K_{th}}{k_B T_e(t)}\right) (\psi K_{th} - \sigma_{1s-4p}), \quad (\text{B3})$$

where $\sigma_{1s-4p} = \frac{4}{K_w^2} \exp\left(\frac{K_{th}}{K_w}\right) K_{th}^4$. Now, we plug the result of the integral in Eq. B3 back into Eq. 4,

$$n_e(t) \langle v_{en}(t) \rangle \approx A' n_e(t) n_n(t) (k_B T_e(t))^{-3/2} k_B T_e(t) \exp\left(-\frac{K_{th}}{k_B T_e(t)}\right), \quad (\text{B4})$$

where A' is a collective constant. To calculate the temporally integrated photon emission, we integrate Eq. B4 from $t = 0$ to $t = \infty$,

$$\int_0^{\infty} n_e(t) \langle v_{en}(t) \rangle dt \approx \int_0^{\infty} A' n_e(t) n_n(t) (k_B T(t))^{-1/2} \exp\left(-\frac{K_{th}}{k_B T(t)}\right) dt. \quad (\text{B5})$$

To continue the calculation, a few assumptions are made: $n_n(t) = n_0$, $k_B T_e(t) \approx k_B T_{e0} e^{-t/\tau_d}$, $n_e(t) \approx n_0 e^{-t/\tau_d}$, where τ_d is the decay lifetime and T_{e0} is the plasma electron temperature before the decay. The first assumption is justified because the neutral particles fill in the plasma column much faster than the full expansion time scale, leading to a quasi-homogenous background of neutral gas. The second and third assumptions are justified by the lineout in Fig. 3(b). So Eq. B5 now becomes

$$\int_0^{\infty} A' n_0^2 e^{-t/\tau_d} (k_B T_{e0} e^{-t/\tau_d})^{-1/2} \exp\left(-\frac{K_{th}}{k_B T_{e0} e^{-t/\tau_d}}\right) dt \approx A' n_0^2 (k_B T_{e0})^{-1/2} 2\tau_d \left(e^{-\frac{K_{th}}{k_B T_{e0}}} - \frac{K_{th} \sqrt{\pi} \text{Erfc}\left(\sqrt{\frac{K_{th}}{k_B T_{e0}}}\right)}{\sqrt{K_{th} k_B T_{e0}}} \right), \quad (\text{B6})$$

where Erfc is the complementary error function, and when $k_B T_{e0} \ll K_{th}$, $\text{Erfc}\left(\sqrt{\frac{K_{th}}{k_B T_{e0}}}\right) \approx 0$. This simplifies Eq. B6 to

$$\int_0^{\infty} n_e(t) \langle v_{en}(t) \rangle dt \approx A' n_0^2 (k_B T_{e0})^{-1/2} 2\tau_d e^{-\frac{K_{th}}{k_B T_{e0}}}, \quad (\text{B7})$$

We empirically find from our simulations that the decay lifetime τ_d is linearly proportional to the initial kinetic energy as shown in Fig. 11. So Eq. B7 becomes

$$\int_0^{\infty} n_e(t) \langle v_{en}(t) \rangle dt \approx 2A' n_0^2 (k_B T_{e0})^{1/2} e^{-\frac{K_{th}}{k_B T_{e0}}}. \quad (\text{B8})$$

Finally, we note that the observed plasma light arises almost entirely from collisions occurring after the initial rapid plasma expansion, so we plug in the temperature after the initial rapid expansion $T_{e0} = RT_0$ where we empirically find $R = 0.09$ from

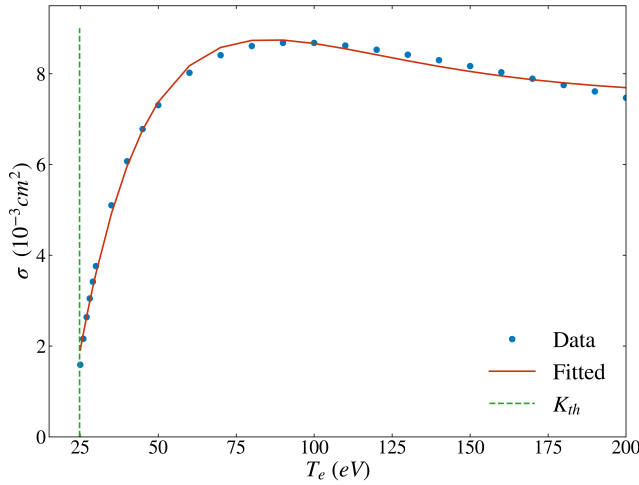


FIG. 10. The electron-impact excitation cross-section of the $1s$ state to the $4p$ state, $\sigma_{1s \rightarrow 4p}$. The blue data points are taken from Ref. 43 and the red curve corresponds to a fit using Eq. B1. The green dashed line denotes the excitation threshold energy, K_{th} .

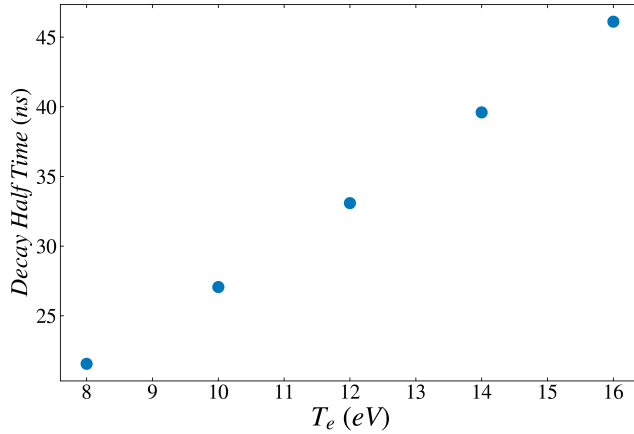


FIG. 11. The peak photon density decay half-life (at $x = 0, y = 0$) for various initial average electron temperatures for a thin, laser ionized PWFA plasma with density $n_e = 8e17 \text{ cm}^{-3}$.

our simulations. Thus, we finally arrive at the following expression of proportionality for the time-integrated peak light emission $n_{\gamma, \text{peak}}$:

$$\Gamma \propto n_0^2 \sqrt{Rk_B T_0} \exp\left(-\frac{K_{th}}{Rk_B T_0}\right). \quad (\text{B9})$$

¹I. Blumenfeld, C. E. Clayton, F. J. Decker, M. J. Hogan, C. Huang, R. Ischebeck, R. Iverson, C. Joshi, T. Katsouleas, N. Kirby, W. Lu, K. A. Marsh, W. B. Mori, P. Muggli, E. Oz, R. H. Siemann, D. Walz, and M. Zhou, “Energy doubling of 42 gev electrons in a metre-scale plasma wakefield accelerator,” *Nature* **445**, 741–744 (2007).

²M. Litos, E. Adli, W. An, C. I. Clarke, C. E. Clayton, S. Corde, J. P. Delahaye, R. J. England, A. S. Fisher, J. Frederico, S. Gessner, S. Z. Green, M. J. Hogan, C. Joshi, W. Lu, K. A. Marsh, W. B. Mori, P. Muggli, N. Vafaei-Najafabadi, D. Walz, G. White, Z. Wu, V. Yakimenko, and G. Yocky,

“High-efficiency acceleration of an electron beam in a plasma wakefield accelerator,” *Nature* **515**, 92–95 (2014).

³M. Litos, E. Adli, J. Allen, W. An, C. Clarke, S. Corde, C. E. Clayton, J. Frederico, S. J. Gessner, S. Green, *et al.*, “9 gev energy gain in a beam-driven plasma wakefield accelerator,” *Plasma Physics and Controlled Fusion* **58** (2016).

⁴X. L. Xu, J. F. Hua, Y. P. Wu, C. J. Zhang, F. Li, Y. Wan, C. H. Pai, W. Lu, W. An, P. Yu, M. J. Hogan, C. Joshi, and W. B. Mori, “Physics of phase space matching for staging plasma and traditional accelerator components using longitudinally tailored plasma profiles,” *Physical Review Letters* **116** (2016).

⁵K. Floettmann, “Adiabatic matching section for plasma accelerated beams,” *Physical Review Special Topics - Accelerators and Beams* **17** (2014).

⁶R. Ariniello, C. E. Doss, K. Hunt-Stone, J. R. Cary, and M. D. Litos, “Transverse beam dynamics in a plasma density ramp,” *Physical Review Accelerators and Beams* **22** (2019).

⁷R. Ariniello, C. E. Doss, V. Lee, C. Hansel, J. R. Cary, and M. D. Litos, “Chromatic transverse dynamics in a nonlinear plasma accelerator,” *Physical Review Research* **4** (2022).

⁸M. Honkanen and J. Turunen, “Tandem systems for efficient generation of uniform-axial-intensityessel fields,” *Optics Communications* **154**, 368–375 (1998).

⁹I. Oudghiri-Idrissi, R. Giust, L. Froehly, M. Jacquot, L. Furfaro, J. M. Dudley, and F. Courvoisier, “Arbitrary shaping of on-axis amplitude of femtosecond bessel beams with a single phase-only spatial light modulator,” *Optics Express* **24**, 11495 (2016).

¹⁰R. Ariniello, *Emittance Preservation in a Plasma Wakefield Accelerator*, Ph.D. thesis, University of Colorado, Boulder (2022).

¹¹V. Lee, J. Moody, G. Demeter, G. Kriehn, P. Muggli, A. Collaboration, *et al.*, “Experimental nonlinear observation of tw laser propagation through a 10m rubidium vapor source for plasma diagnostics at awake,” *Conference on Lasers and Electro-Optics, OSA Technical Digest*, FTh1B–3 (2019).

¹²A. Newton and M. Sexton, “The decay of a highly ionized helium plasma,” *Journal of Physics B: Atomic and Molecular Physics* **1**, 669 (1968).

¹³R. J. Shalloo, C. Arran, L. Corner, J. Holloway, J. Jonnerby, R. Walczak, H. M. Milchberg, and S. M. Hooker, “Hydrodynamic optical-field-ionized plasma channels,” *Physical Review E* **97** (2018).

¹⁴“Laser induced plasma expansion and existence of local thermodynamic equilibrium,” *Spectrochimica Acta - Part B Atomic Spectroscopy* **125**, 103–110 (2016).

¹⁵M. Capitelli, A. Casavola, G. Colonna, and A. D. Giacomo, “Laser-induced plasma expansion: Theoretical and experimental aspects,” *Spectrochimica Acta - Part B Atomic Spectroscopy* **59**, 271–289 (2004).

¹⁶C. Zhang, C. K. Huang, K. A. Marsh, and C. Joshi, “Probing thermal weibel instability in optical-field-ionized plasmas using relativistic electron bunches,” *Plasma Physics and Controlled Fusion* **62** (2020).

¹⁷C. Zhang, J. Hua, Y. Wu, Y. Fang, Y. Ma, T. Zhang, S. Liu, B. Peng, Y. He, C. K. Huang, K. A. Marsh, W. B. Mori, W. Lu, and C. Joshi, “Measurements of the growth and saturation of electron weibel instability in optical-field ionized plasmas,” *Physical Review Letters* **125** (2020).

¹⁸G. Baravian, R. Benattar, J. Bretagne, J. L. Godart, and G. Sultan, “Electron-ion recombination in a helium plasma produced by laser,” *Z. Physik* **254**, 218–231 (1972).

¹⁹D. R. Bates, A. E. Kingston, and R. W. P. McWhirter, “Recombination between electrons and atomic ions. i. optically thin plasmas,” *Proceedings of the Royal Society of London. Series A. Mathematical and Physical Sciences* **267**, 297–312 (1962).

²⁰C. Joshi, E. Adli, W. An, C. E. Clayton, S. Corde, S. Gessner, M. J. Hogan, M. Litos, W. Lu, K. A. Marsh, W. B. Mori, N. Vafaei-Najafabadi, B. O’Shea, X. Xu, G. White, and V. Yakimenko, “Plasma wakefield acceleration experiments at facet ii,” *Plasma Physics and Controlled Fusion* **60** (2018).

²¹A. Deng, O. S. Karger, T. Heinemann, A. Knetsch, P. Scherkl, G. G. Manahan, A. Beaton, D. Ullmann, G. Wittig, A. F. Habib, Y. Xi, M. D. Litos, B. D. O’Shea, S. Gessner, C. I. Clarke, S. Z. Green, C. A. Lindström, E. Adli, R. Zgadzaj, M. C. Downer, G. Andonian, A. Murokh, D. L. Bruhwiler, J. R. Cary, M. J. Hogan, V. Yakimenko, J. B. Rosenzweig, and B. Hidding, “Generation and acceleration of electron bunches from a plasma photocathode,” *Nature Physics* **15**, 1156–1160 (2019).

- ²²E. Adli, C. A. Lindstrom, J. Allen, C. I. Clarke, J. Frederico, S. J. Gessner, S. Z. Green, M. J. Hogan, M. D. Litos, B. O'Shea, V. Yakimenko, W. An, C. E. Clayton, K. A. Marsh, W. B. Mori, C. Joshi, N. Vafaei-Najafabadi, S. Corde, and W. Lu, "Long-range attraction of an ultrarelativistic electron beam by a column of neutral plasma," *New Journal of Physics* **18** (2016).
- ²³P. S. M. Claveria, X. Davoine, J. R. Peterson, M. Gilljohann, I. Andriyash, R. Ariniello, C. Clarke, H. Ekerfelt, C. Emma, J. Faure, S. Gessner, M. J. Hogan, C. Joshi, C. H. Keitel, A. Knetsch, O. Kononenko, M. Litos, Y. Mankovska, K. Marsh, A. Matheron, Z. Nie, B. O'Shea, D. Storey, N. Vafaei-Najafabadi, Y. Wu, X. Xu, J. Yan, C. Zhang, M. Tamburini, F. Fiuza, L. Gremillet, and S. Corde, "Spatiotemporal dynamics of ultrarelativistic beam-plasma instabilities," *Physical Review Research* **4** (2022).
- ²⁴L. D. Amorim and N. Vafaei-Najafabadi, "Ionization injection of 'inception' beams in plasma wakefield accelerators," *Plasma Physics and Controlled Fusion* **61** (2019).
- ²⁵S. Corde, E. Adli, J. M. Allen, W. An, C. I. Clarke, B. Clausse, C. E. Clayton, J. P. Delahaye, J. Frederico, S. Gessner, S. Z. Green, M. J. Hogan, C. Joshi, M. Litos, W. Lu, K. A. Marsh, W. B. Mori, N. Vafaei-Najafabadi, D. Walz, and V. Yakimenko, "High-field plasma acceleration in a high-ionization-potential gas," *Nature Communications* **7** (2016).
- ²⁶C. E. Doss, E. Adli, R. Ariniello, J. Cary, S. Corde, B. Hidding, M. J. Hogan, K. Hunt-Stone, C. Joshi, K. A. Marsh, J. B. Rosenzweig, N. Vafaei-Najafabadi, V. Yakimenko, and M. Litos, "Laser-ionized, beam-driven, underdense, passive thin plasma lens," *Physical Review Accelerators and Beams* **22** (2019).
- ²⁷L. Keldysh *et al.*, "Ionization in the field of a strong electromagnetic wave," *Sov. Phys. JETP* **20**, 1307–1314 (1965).
- ²⁸P. Stoffa, J. T. Fokkema, R. de Luna Freire, and W. Kessinger, "Split-step fourier migration," *Geophysics* **55**, 410–421 (1990).
- ²⁹C. Nieter and J. R. Cary, "Vorpil: a versatile plasma simulation code," *Journal of Computational Physics* **196**, 448–473 (2004).
- ³⁰L. Spitzer, *Physics of Fully Ionized Gases Interscience Publishers* (1962) p. 28.
- ³¹M. Brio and C. C. Wu, "An upwind differencing scheme for the equations of ideal magnetohydrodynamics," *Journal of Computational Physics* **75**, 400–422 (1988).
- ³²E. T. Meier and U. Shumlak, "A general nonlinear fluid model for reacting plasma-neutral mixtures," *Physics of Plasmas* **19** (2012).
- ³³V. H. Chaplin and P. M. Bellan, "One-dimensional time-dependent fluid model of a very high density low-pressure inductively coupled plasma," *Journal of Applied Physics* **118** (2015).
- ³⁴V. Vahedi and M. Surendra, "A monte carlo collision model for the particle-in-cell method: applications to argon and oxygen discharges," *Computer Physics Communications* **87**, 179–198 (1995).
- ³⁵C. E. Theodosiou, "Atomic data and nuclear data table," **36** (1987).
- ³⁶J. B. Boffard, C. C. Lin, and C. A. DeJoseph, "Application of excitation cross sections to optical plasma diagnostics," *Journal of Physics D: Applied Physics* **37** (2004).
- ³⁷Y. Ralchenko, R. K. Janev, T. Kato, D. V. Fursa, I. Bray, and F. J. de Heer, "Electron-impact excitation and ionization cross sections for ground state and excited helium atoms," *Atomic Data and Nuclear Data Tables* **94**, 603–622 (2008).
- ³⁸Y. Hahn, "Electron-ion recombination processes-an overview," *Reports on Progress in Physics* **60**, 691 (1997).
- ³⁹H. Drawin and F. Emard, "Comparative study of existing theories for volume ion-electron recombination in plasmas," *Beitraege aus der Plasma-physik* **15**, 273–290 (1975).
- ⁴⁰J. D. Huba, *NRL plasma formulary*, Vol. 6790 (Naval Research Laboratory, 1998).
- ⁴¹F. F. Chen *et al.*, *Introduction to plasma physics and controlled fusion*, Vol. 1 (Springer, 1984).
- ⁴²S. Ma, J. Howard, and N. Thapar, "Relations between light emission and electron density and temperature fluctuations in a helium plasma," *Physics of Plasmas* **18** (2011).
- ⁴³P. M. Stone, Y.-K. Kim, and J. Desclaux, "Electron-impact cross sections for dipole- and spin-allowed excitations of hydrogen, helium, and lithium," *Journal of research of the National Institute of Standards and Technology* **107**, 327 (2002).
- ⁴⁴D. D. Hickstein, S. T. Gibson, R. Yurchak, D. D. Das, and M. Ryazanov, "A direct comparison of high-speed methods for the numerical abel transform," *Review of Scientific Instruments* **90**, 065115 (2019).
- ⁴⁵H. Griem, M. Baranger, A. Kolb, and G. Oertel, "Stark broadening of neutral helium lines in a plasma," *Physical Review* **125**, 177 (1962).
- ⁴⁶Y. Wan, O. Seemann, S. Tata, I. A. Andriyash, S. Smartsev, E. Kroupp, and V. Malka, "Direct observation of relativistic broken plasma waves," *Nature Physics* **18**, 1186–1190 (2022).
- ⁴⁷P. Scherkl, A. Knetsch, T. Heinemann, A. Sutherland, A. F. Habib, O. S. Karger, D. Ullmann, A. Beaton, G. G. Manahan, Y. Xi, A. Deng, M. D. Litos, B. D. O'Shea, S. Z. Green, C. I. Clarke, G. Andonian, R. Assmann, D. L. Bruhwiler, J. Smith, J. R. Cary, M. J. Hogan, V. Yakimenko, J. B. Rosenzweig, and B. Hidding, "Plasma photonic spatiotemporal synchronization of relativistic electron and laser beams," *Physical Review Accelerators and Beams* **25** (2022).
- ⁴⁸R. D'Arcy, J. Chappell, J. Beinortaita, S. Diederichs, G. Boyle, B. Foster, M. J. Garland, P. G. Caminal, C. A. Lindström, G. Loisch, *et al.*, "Recovery time of a plasma-wakefield accelerator," *Nature* **603**, 58–62 (2022).
- ⁴⁹S. Diederichs, C. Benedetti, E. Esarey, M. Thévenet, A. Sinn, J. Osterhoff, and C. B. Schroeder, "Temperature effects in plasma-based positron acceleration schemes using electron filaments," *Physics of Plasmas* **30**, 073104 (2023).
- ⁵⁰Y. Ma, D. Seipt, A. Hussein, S. Hakimi, N. Beier, S. Hansen, J. Hinojosa, A. Maksimchuk, J. Nees, K. Krushelnick, *et al.*, "Polarization-dependent self-injection by above threshold ionization heating in a laser wakefield accelerator," *Physical Review Letters* **124**, 114801 (2020).
- ⁵¹B. Miao, J. Shrock, L. Feder, R. Hollinger, J. Morrison, R. Nedbailo, A. Picksley, H. Song, S. Wang, J. Rocca, *et al.*, "Multi-gev electron bunches from an all-optical laser wakefield accelerator," *Physical Review X* **12**, 031038 (2022).
- ⁵²F. Robben, W. B. Kunkel, and L. Talbot, "Spectroscopic study of electron recombination with monatomic ions in a helium plasma," *Physical Review* **132**, 2363 (1963).